TESTING PROTOCOL DEVELOPMENT FOR FRACTURE TOUGHNESS OF PARTS BUILT WITH BIG AREA ADDITIVE MANUFACTURING

J. P. Garcia [a b], L. A. Camacho [a b], A. Hasanyana [a], D. Espalin [a b]

[a] Department of Aerospace and Mechanical Engineering, The University of Texas at El Paso, 500 W. University Ave. El Paso, Texas, 79968

[b] W.M. Keck Center for 3D Innovation, 500 W. University Ave. El Paso, Texas, 79968

1 Abstract

Mechanical testing of additively manufactured parts has largely relied on existing standards developed for traditional manufacturing. While this approach leverages the investment made on current standards development, it inaccurately assumes that mechanical response of AM parts is identical to that of parts manufactured through traditional processes. When considering thermoplastic, material extrusion AM, differences in response can be attributed to an AM part's inherent inhomogeneity caused by porosity, interlayer zones, and surface texture. Additionally, interlayer bonding of parts printed with large-scale AM is difficult to adequately assess as much testing is done such that stress is distributed across many layer interfaces; therefore, the lack of AM-specific standard to assess interlayer bonding is a significant research gap. To quantify interlayer bonding via fracture toughness, double cantilever beam (DCB) testing has been used for some AM materials, and DCB has been generally used for a variety of materials including metal, wood, and laminates. Mode I DCB testing was performed on thermoplastic matrix composites printed with Big Area Additive Manufacturing (BAAM). Of particular interest was the crack shape and deflection speed during testing. A modernization of the testing process was proposed using visual processing of a recording of the crack propagation to get more accurate calculations. Results discuss the differences when using two crack types and three deflection speeds.

2 Introduction

Although additive manufacturing technology is advancing at great lengths, there is a considerable lack of standards for characterizing mechanical properties of Additive Manufacturing (AM) materials. It is important to mention that though a lack of standards exists for characterizing interlayer bonding, there are efforts to compile standards that serve as the basis for testing AM materials. The focus of this project is mechanical characterization of material extrusion (MEX) composites for large-scale additive manufacturing.

It is known that for traditionally manufactured composite materials with a polymer matrix, the materials are anisotropic in their mechanical properties, something also true for parts built with MEX. Important factors to be considered for material characterization for composites are fiber orientation, fiber continuity and stacking sequence. In literature it is established that in large-scale AM there is some alignment of the short fibers to the printing direction on the x/y plane at the layer interface [8, 21, 35]. Assuming that fiber orientation on the print was largely

unidirectional, the search for a standard was focused on one that called for unidirectional fibers within composite materials, the selected standard was Double Cantilever Beam (DCB). Something to consider is that one of the DCB standards most consulted for the project called for digital image correlation, a feature already implemented in mechanical testing for Large-Area AM. An example being the work done by Schnittker et al. [29] which the use of digital imaging and the printing of a hexagonal shape for coupon extraction, the current project took inspiration from. It is also important to note that after dispensing, the material shrinks and deforms adding a layer of complexity to fiber orientation, called nesting [11], which is important to observe as it may impact the interaction at the layer interface. The stacking sequence for each layer is assumed to be at 0° with the reference axis being the printing direction and that fibers are either short or discontinuous at the layer interface of a print, as observed in Figure 1.
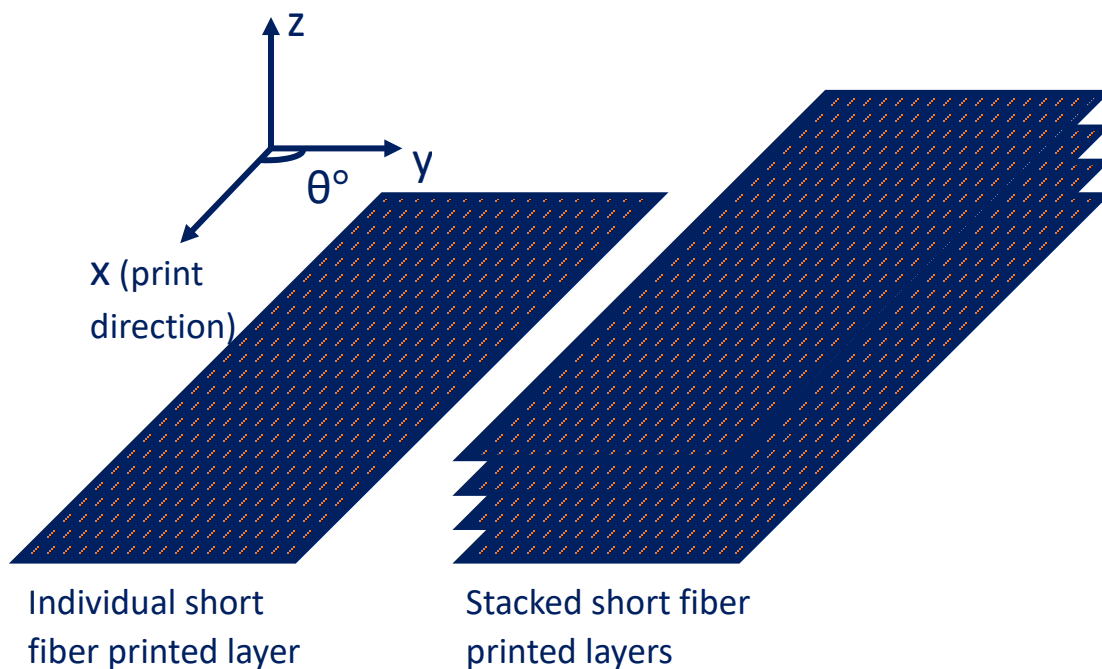
Figure 1 Matrix/Fiber relation at the print's layer interface

The examination of fracture toughness in additive manufacturing (AM), particularly in large-scale AM, is limited in scope. This investigation specifically focuses on characterizing fracture toughness at the interlayer level, which serves as an indicator of the strength of bonds between layers. By shedding light on the material's capabilities and assessing its controllability in this aspect, it enables further customization for specific applications. Moreover, it establishes a foundation for future standardization efforts in additive manufacturing, encompassing specialized specimen geometries. In addition to bridging existing knowledge gaps, this paper introduces a pioneering approach to recording fracture toughness data. A MATLAB script was developed to process both video and test data post-experiment, enhancing the analysis process.

3 Methodology
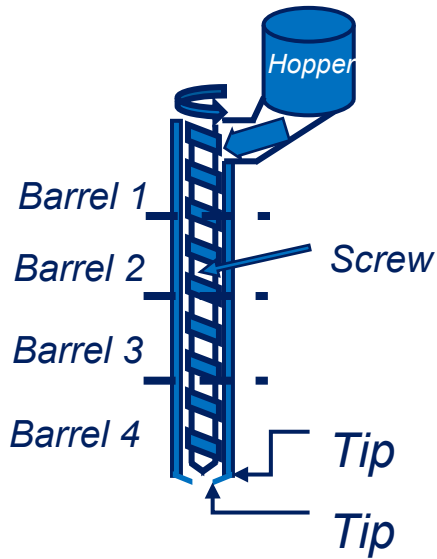
3.1 Coupon Fabrication

Figure 2: Heated zones and hopper system for the extruder

For the experiment, the material used was Electrafil® ABS 1501 3DP (Techmer PM, Wichita, Kansas, USA), which was 20 wt.% carbon filled ABS. The CF-ABS was dried for four hours at 90° C before extrusion. The material was extruded at 245° C being heated continuously inside the barrel from Figure 2 from 190, 205, 245 and 245 per zone respectively. The geometry used for the harvesting of coupons was a single wall hexagon with a wall length of 304.8 mm and a height of 217.51 mm. The slicer used was ORNL Slicer 2 version 2 with a layer height of 3.5 mm (Oak Ridge National Labs, Oak Ridge, Tennessee, USA). A hexagonal shape [29] was chosen so the six panels were printed with minimal deformation and in similar printing conditions. Each panel in turn was designed to yield six coupons for an adequate number of testing samples (Figure 3). The samples were printed using a Big Area Additive Manufacturing (BAAM) developed by Cincinnati and Oakridge National Laboratory (ORNL).

Figure 3: Double Cantilever nomenclature diagram

To harvest the coupons the panels were cut from the hexagon using water jetting. Water jetting was decided over hacksaw or horizontal band saw because is less thermally invasive to the coupon. The geometry of the sample (Figure 4) was selected following the practical requirements of the testing. Specific dimensions were selected by deferent criteria. Length of the coupon was chosen due to the limitations of the testing rig (Instron 5866, Instron, Norwood,

Massachusetts, USA) while the height was selected to prevent transversal cracking. The most critical geometry feature is the point at which the load is applied and the tip of the pre-crack which is defined by (a_o), the symmetry of the specimen along the fracture plane and interlayer width.
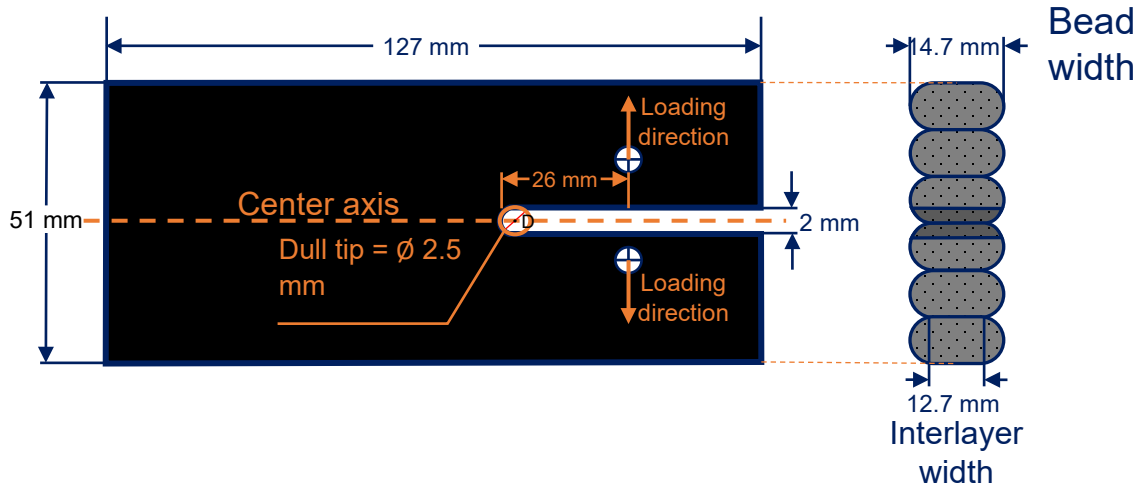

Figure 4: DCB sample geometry

After fabrication, each sample went through a labeling process. The coupons were labeled with a number from 1 to 6 corresponding to the face of the hexagon they belonged to. The numbers were accompanied by a letter from A to F in accordance to the positioning of the coupon within the panel (Figure 3). Additionally, for testing the coupons were conditioned with the help of the reference of ASTM standard D618 which goes into detail of conditioning procedures. It was stated on the standard to store and test at a laboratory atmosphere of 23 °C ± 3 °C in temperature and 50 ± 10% relative humidity for a minimum of 88 hours [5].

3.2 Double Cantilever Testing

The Instron 5866 was fitted with a 10 kN 2525 load cell for the testing, while the Bluehill2 software (Instron, Norwood, Massachusetts, USA) was used to record load and crosshead displacement. To correlate the load/displacement curves with the specimen's specific crack length, video recording was used. The equipment selected for the video recording was a Canon EOS 80D camera equipped with a Canon EF 10mm f/2.8L Macro IS USM lens CA (Canon, Melville, New York, USA). The information gathered from the Instron and the camara was used to calculate fracture toughness.
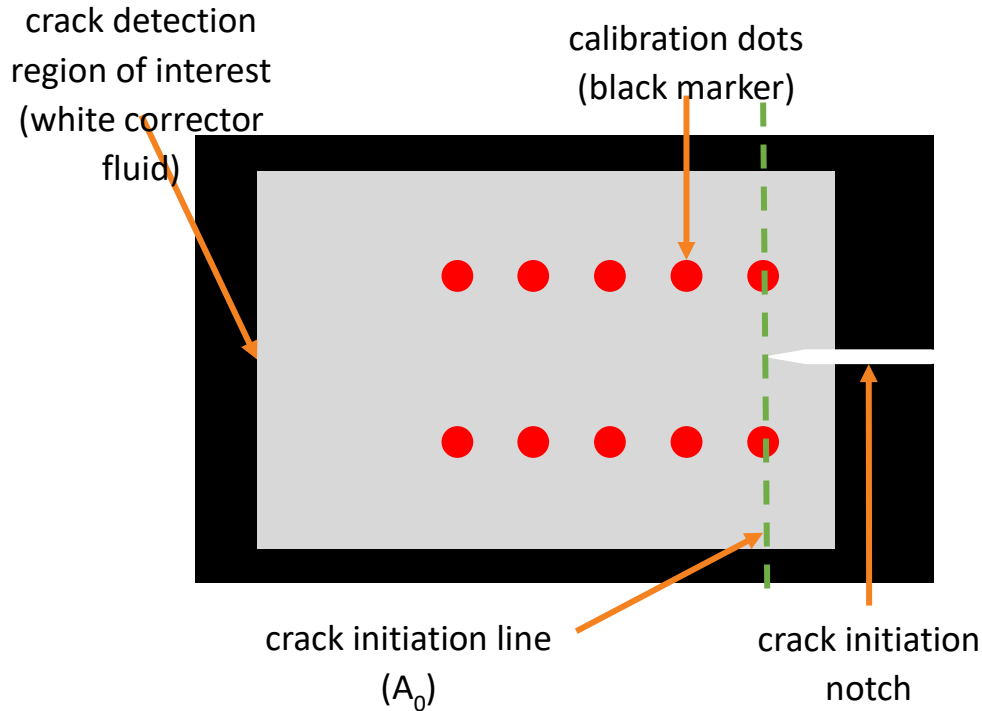
Figure 5: Specimen requirement for software

Prior to testing, interlayer width was measured for every specimen. After the measurement a thin layer of white corrector fluid was applied as a coating for the specimens. A custom stencil was used to add the calibration marks on top of the coating (Figure 5). For the experiment, as load was applied to the specimen the camera recorded the length crack propagation. A separate recording pointed at the Bluehill2 software was used so both recordings can be synchronized and a relationship between experimental load and displacement with the recorded crack length can be established using the frames of the recording. The OBS studio software was used to synchronize both recordings (Figure 6). This technique allowed to gather hundreds of points in the crack length. As mentioned before, the specimen surfaces were marked with calibration dots consisting in two parallel rows which in turn were parallel to the pre-crack. Each row had eleven dots with a nominal distance of 5mm between them. It is of importance to mention that the stencil used for marking the dots was manufactured using vat photopolymerization which carries dimensional inaccuracies which were compensated for at the printing parameter and code stages. The dots were useful to correct distortion, to average the distance between adjacent dots and maintaining a consistent aspect ratio as well as giving a general idea on the state of the image surrounding each dot.
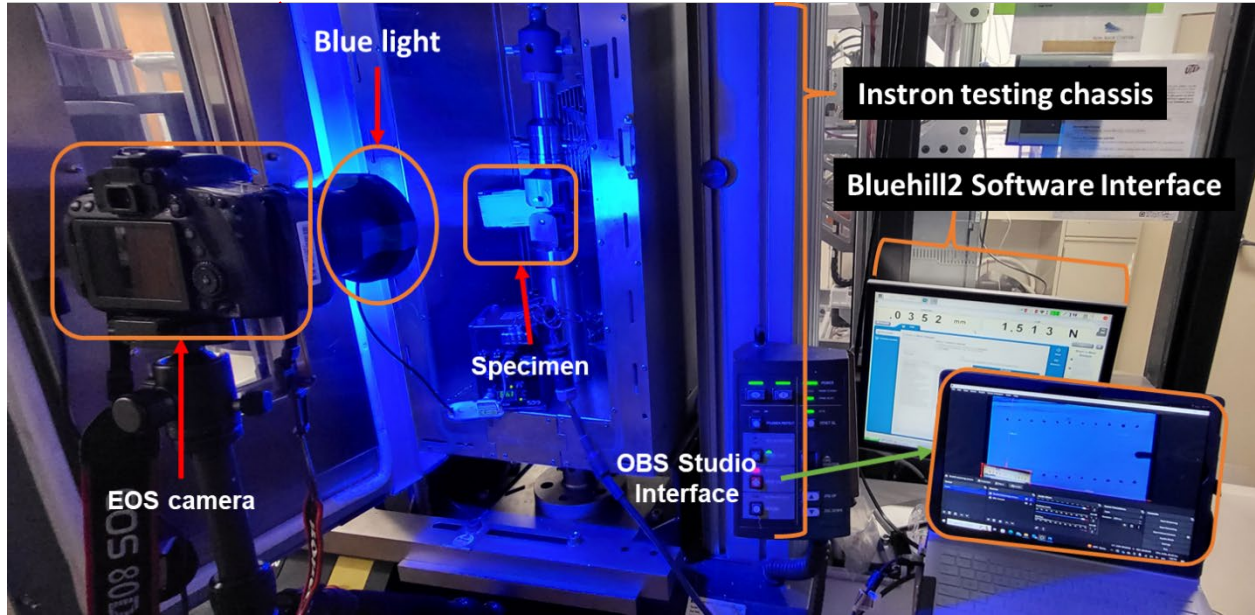
Figure 6: DCB Experimental setup

The experimental setup consisted of the Canon EOS 80D camera being placed normal to the specimen's crack propagation surface (Figure 6). A blue light was shined towards the white cover of the specimen for higher contrast between painted parts and the crack, background, and unpainted parts for image processing. Two batches of specimens were prepared in different ways, the first batch was tested with a small semicircle ending the pre-crack notch, while the second batch had an incision made with tungsten carbide box cutter razorblades (DeWalt, Towson, Maryland, USA). The objective of the difference between pre-crack notches was to verify that by making the pre-crack notch ending thinner, instead of testing structural strength, the material properties would be tested. Apart from the specimens having a razor pre-crack or lacking it, six specimens were tested at a speed of 5 mm/min with and without preloading with preloading describing the process at which the specimen is exposed to enough loading to propagate the crack from 3 to 5 mm from the pre-crack tip.

3.2 Image Processing

For image processing MATLAB was used to extract frames and process them for correlation between frames and load/displacement and then record the data for each test. The MATLAB process has a four-part workflow consisting of frame and data extraction, image calibration, crack propagation measurements and fracture toughness calculations. The novelty of the process explained in this paper lies in frame extraction, calibration and crack propagation which will be explained in conjunction.

For the data acquisition, the test video was recorded at 60 frames per second while the load/displacement data was recorded every 0.334 s. The timelapse for data acquisition was deliberate since 0.334 s is a multiple of 60 frames per second. This is useful to extract frames that are consistent in relation to data and frames both the crack propagation video and the screen

recording from the Bluehill2 software load/displacement were merged into a single recording using OBS Studio. The video was then trimmed, using a computer default editor to view, from the start of the testing to the end of the test. Per every load/displacement data point, a frame would be collected equidistantly in relation to time by MATLAB. A crucial part of data acquisition was calibration. The intention of calibration was to size the pixels in terms of millimeters. The calibration method uses two rows of dots at the top and at the bottom of the crack, instead of a single gauge length (two dots) to find the pixel size ratio. Since the image resolution for every frame is the same, just one frame is needed for calibration. The frame selected for calibration was at which the specimen had reached critical load, thus named critical load frame. The critical frame was selected because, at this point of the testing, rotation from the initial loading reached stability and sat before crack propagation where rotation from crack opening occurs. The workflow for calibration then consists of using the script to find the dots as circles and calculate the distance between the adjacent circle centers. These distances were intended to be 5mm between circle to circle thus the number of pixels between each circle center was divided by this distance giving a mm/pixel ratio. Since the positioning of the specimen might had changed from set up to set up, this method allowed for an undesirable tilt, which was compensated for by creating a linear regression per each row of dots (top and bottom) and using the average slope of both sides to compensate as the crack length propagated. The first few frames were neglected for the calculation since the crack length remained the same as the initial pre-crack, a_o. Additionally, since the lens used on the camera for the testing was a narrow lens, distortion was negligible.
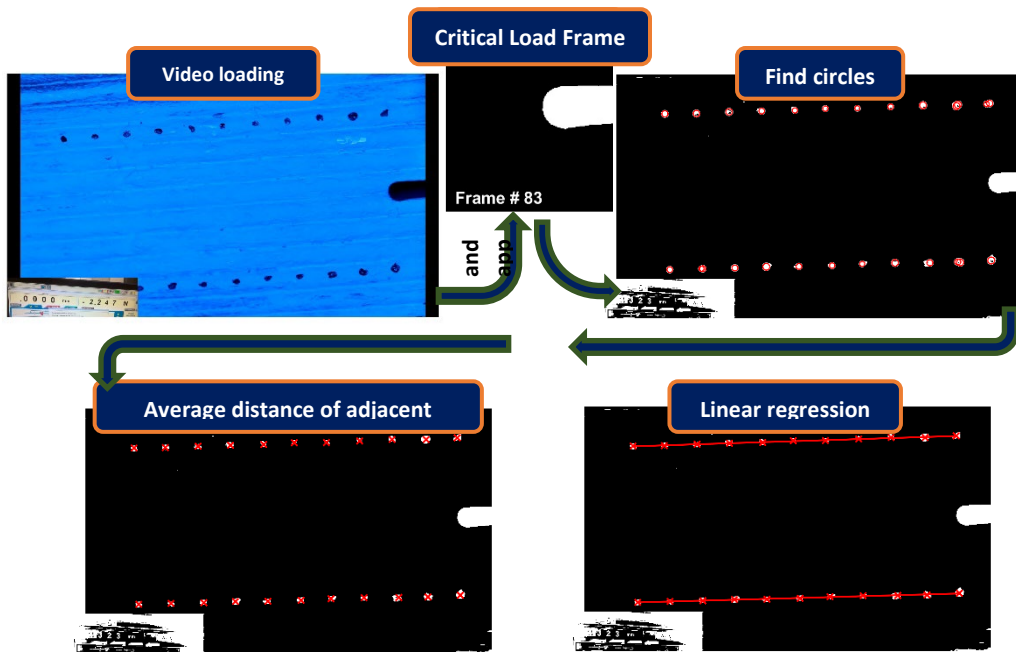

Figure 7: Calibration subsection workflow

The formula used to calculate fracture toughness (G_{IC})(Eq.1) [23] compensates for shear loading and rotation happening throughout the crack propagation as well as offsetting to account

for beam rotation already shows the plotted curve depicting load versus deflection, referred to as the corrected load versus deflection (LvD) plot in this study's script, displayed certain characteristics. Prior to mounting the specimen, the load cell underwent calibration. However, upon mounting the specimen, there remained a small distance that needed to be covered before the load was applied. This additional deflection was deemed irrelevant to the testing process. It is worth noting that these correction methods are not specified in the DCB standard [3]. The decision to offset the values occurred when the linear region intersected the origin. This approach aimed to measure the distance at which loading onto the specimen commenced, rather than considering the deflection range where opening did not impose a load on the specimen. In Figure 8, point A represents the test's initiation, while line BC represents the regression of the LvD plot's linear region. In this scenario, B denotes the new offset length indicating the starting point of loading in the DCB test.

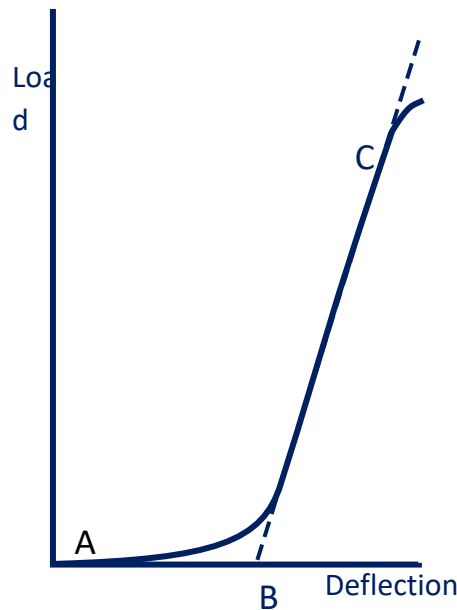$$G_{IC} = \frac{4P_c^2}{Eb^2h^3}[3(a + a_0)^2 + h^2] \qquad (1)$$

Figure 8: LvD offset correction method.

4 Results

Testing was divided into two parts to qualify differences in testing techniques. These two testing blocks consisted of sharpened pre-crack versus unsharpened pre-crack respectively. The goal of the difference between testing techniques is to determine if any difference can have an impact on the testing. The theory behind sharpening the crack is that a dull pre-crack would test for structure instead of material properties. During the initial round of tests (depicted in Figure 8 c and d), an abrupt and nearly vertical crack emerged right after reaching the critical load. This

occurrence is referred to as an unstable brittle fracture. In literature it is clarified that such a situation is unfavorable for detecting fracture toughness. In contrast to the specimen with a sharpened crack tip, the specimen with a dull pre-crack can withstand a higher load (shown in Figure 9 a and b). This dissimilarity arose from structural factors. Lower stress concentration at the pre-crack tip was attributed to the dull water jetted notch fabrication which distributes the load.
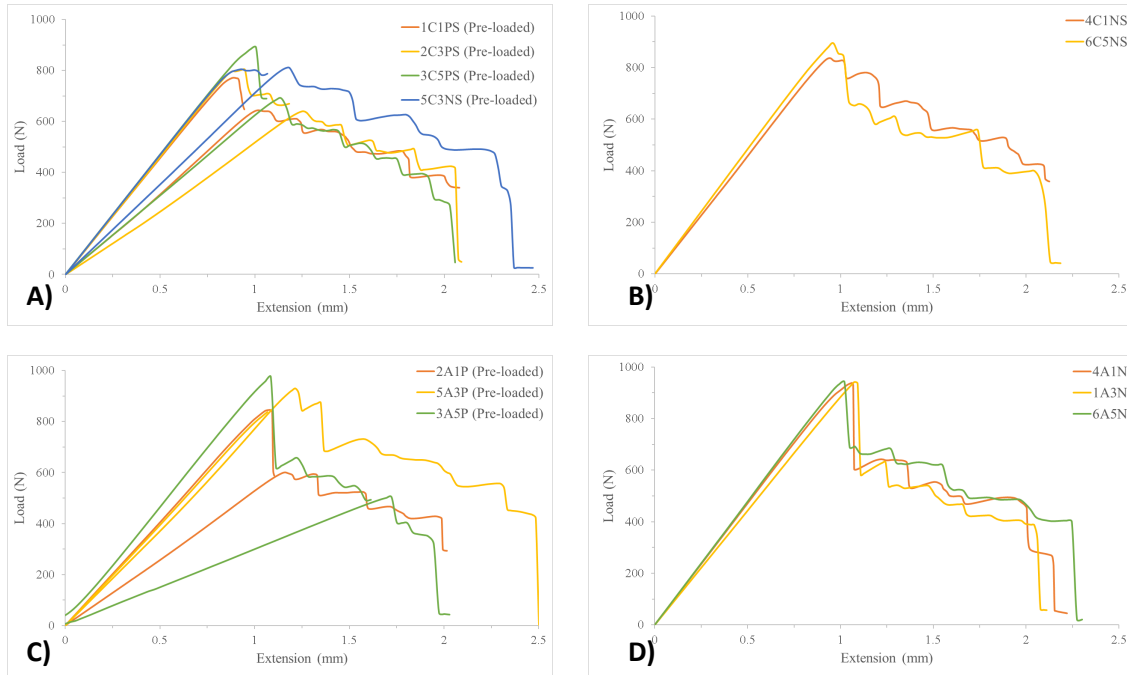

Figure 9: Load versus Extension (crosshead deflection) curve A) pre-loaded samples with crack sharpening B) no-pre-loaded samples with no crack sharpening C) pre-loaded samples D) no-pre-loaded samples

Figure 12 reveals the presence of outliers in the G_{IC} results. While some of these outliers occurred towards the end of the test (Figure 10), they did not manifest consistently for all specimens hindering the interpretations of the results gathered. This discrepancy can be attributed to the specific crack length at which the test had to be manually stopped. At that time, there was no established parameter in the testing software to automatically halt the tests, needing manual intervention. This means certain tests were successfully stopped at the desired crack length, while others experienced catastrophic failure before the operator could stop the test leading to several situations that made each data set different requiring filtering. Catastrophic behavior affects the measurements because of two significant phenomena that can occur. Firstly, the crack extends beyond the frame captured by the camera used for crack length measurements. This occurrence hampers accurate measurement of the crack length. Secondly, the specimen undergoes extreme rotation due to the sudden release of energy, which can be referred to as the point of specimen instability. In the latter event, even if the crack remained within the camera frame, the measurements would still be unreliable due to the excessive rotation and instability of

the specimen. Consequently, accurate fracture toughness calculations cannot be obtained under these conditions.
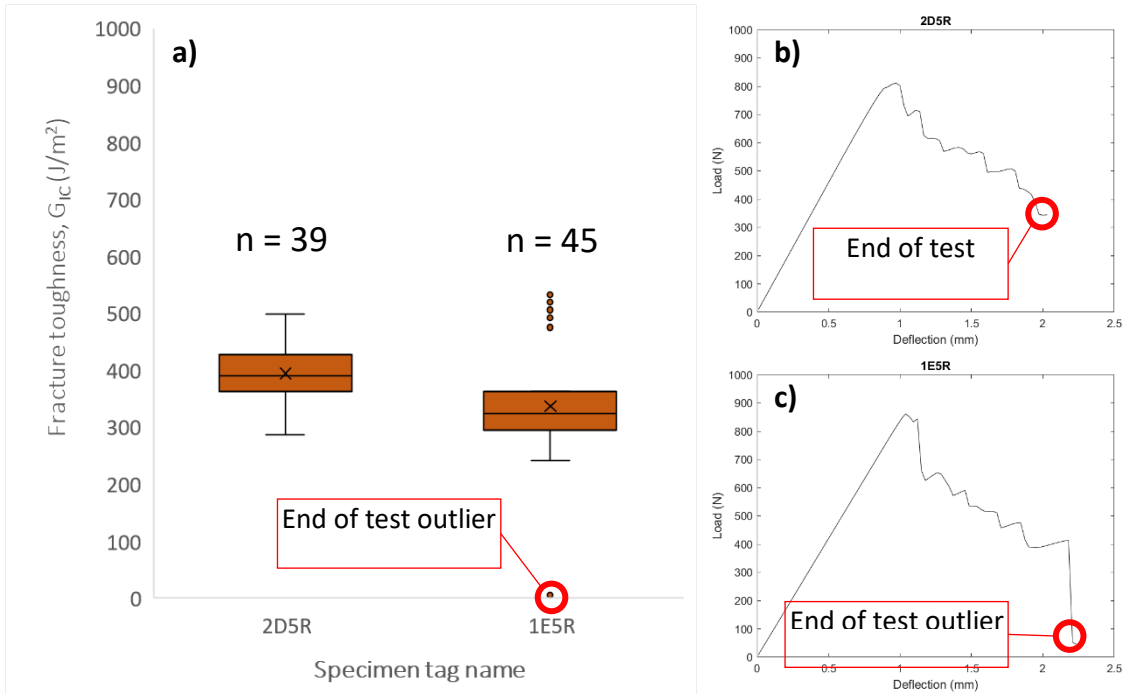

Figure 10: a) Box plot unfiltered values comparison between b) test stopped at the required crack length against c) test stopped after critical failure.
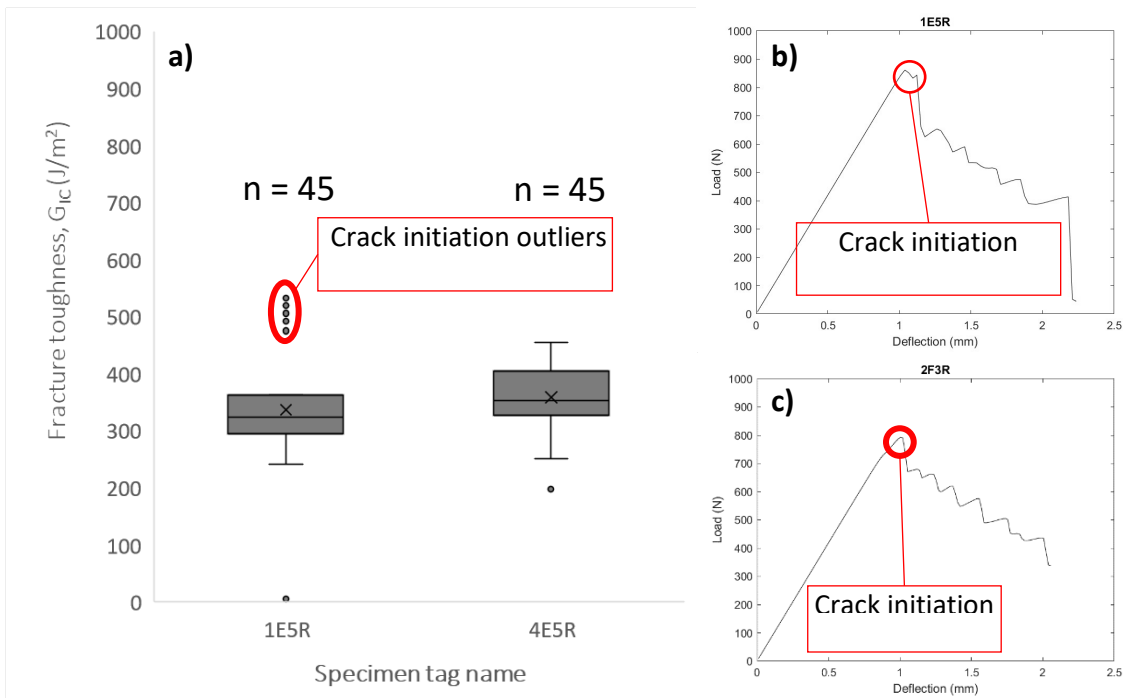

Figure 11: a) Box plot unfiltered values comparison between b) test of low flow impact crack sharpening and b) high impact crack sharpening.

The presence of additional outliers was observed at the onset of crack propagation, specifically at the critical load section of the test (Figure 11). These outliers consistently lead to an overestimation of fracture toughness and manifest in all specimens to varying extents. This phenomenon arises due to the ineffectiveness of the intended impact of crack tip sharpening. In some cases, it appeared as if the crack tip was not sharpened at all when comparing these instances to the critical loads observed in the exploratory work conducted with unsharpened crack tips (Figure 9 c & d). Figure illustrates the extremes of the diverse impact resulting from crack tip sharpening. In Figure 9 b, the impact was lower than intended, while in Figure 9 c, the impact aligned more closely with the desired outcomes. Although the loading behavior returned to normal after the initial crack, the initial crack length in cases of low impact crack tip sharpening extended significantly. This means that the number of useful crack points for analyzing crack propagation decreased.
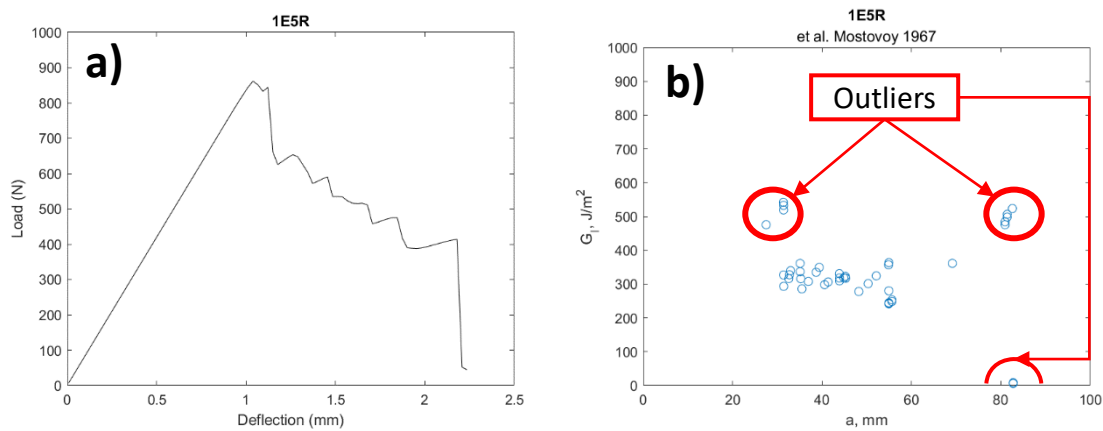

Figure 12: Unfiltered values of a) LvD and b) R-plot of specimen 1E5R

Apart from the outliers observed at the beginning and end of crack propagation, there are additional data points that deviate from the representative behavior of the material. These data points exhibited a downward trend and approached a vertical orientation as the crack propagated. To address these issues, the results underwent filtering by considering only the peak values in the load versus deflection (LvD) graph for fracture toughness calculations (Figure 12). This filtering process helped eliminate the deviations. Since some of the outliers visible at the beginning of the test are also peak values corresponding to the critical load, any peak value occurring at the critical load deflection length or before it was excluded from the calculations. This was achieved by indexing the critical point and creating an array within the software that includes only the values recorded after the critical index. Figure 9 a) shows the LvD plots showing the peaks utilized for calculating the G_{IC} (critical fracture toughness mode I) values for a single specimen as the crack propagates. These plots were accompanied by their respective R-plots (Figure 13) generated using the rigid specimen compliance calibration (RSCC) fracture toughness calculation method. This discriminatory approach was primarily employed to remove outliers from the fracture toughness calculations, as explained previously. RSCC results were grouped together at the box plot from Figure 14.
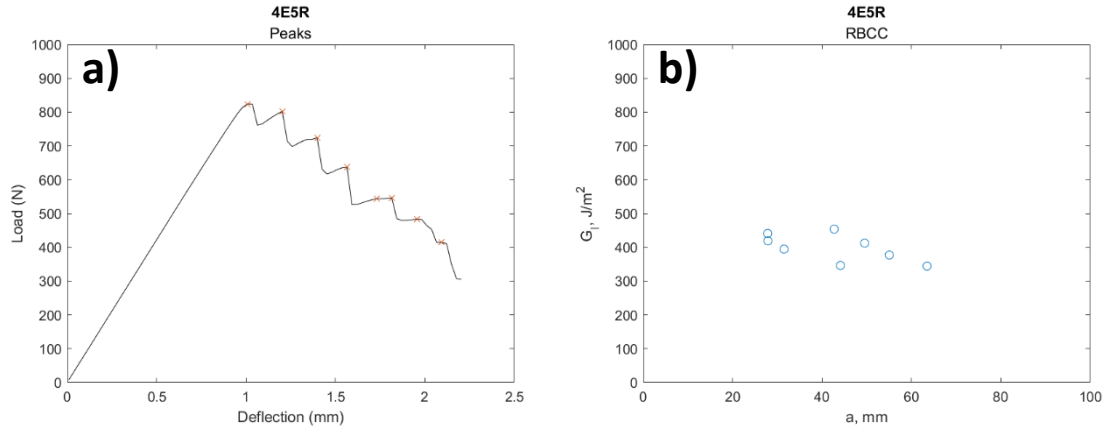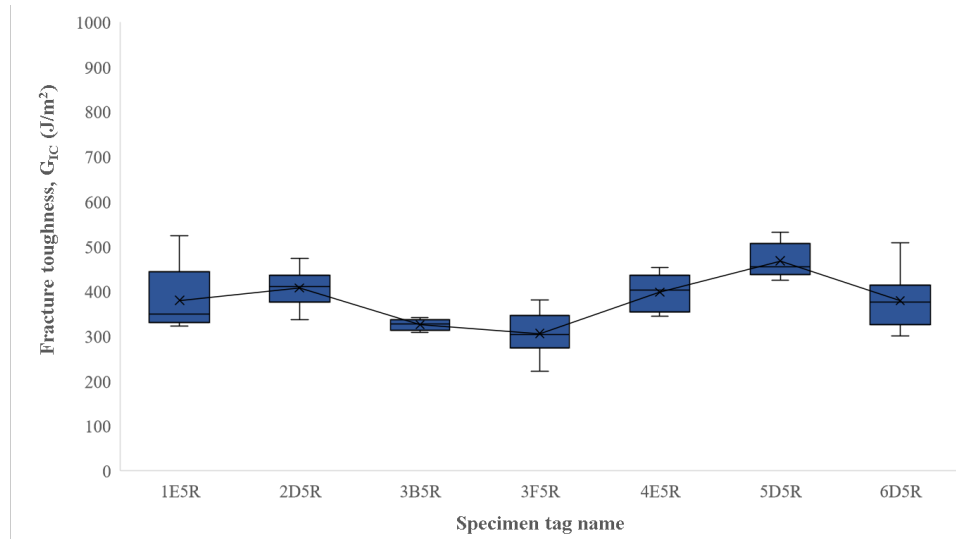
Figure 6: a) R-plot and b) peak values

Figure 14: Fracture toughness, GIC, filtered values of specimens, using RSCC model.

5 Conclusion

The preload vs no preload phases of the project demonstrated no difference between preload and no pre-load. It can be argued that adding pre-load to the testing process could be enhanced by taking some or all human error associated with the process by either automation or improved control techniques, but it was determined to be more practical just to leave the preload out of the process.

Another finding from the project was that sharpening the pre-crack tip led to better results not only at the start of the testing but throughout the crack propagation. The main distinction being that without sharpening, the pre-crack could withstand higher loading testing for structure rather than for material properties. In this study a difference of 100 N, representing a 10%

increase, was observed between the sharpened and unsharpened pre-cracks. A non-sharpened crack tip specimen exhibits a transition from unstable brittle fracture to stable brittle fracture, while sharpened crack tips maintain a brittle stable fracture throughout. This suggests that the dull crack tip distributes the load along the specimen's contour, recording the structural properties rather than the material properties of the specimens. Another observation made is that ineffective crack tip sharpening has an impact on fracture toughness results. As a result of an untreated crack tip, there was a downward trend in crack propagation. It is of relevance to mention that no increase in fracture toughness was observed as the crack propagated, indicating the absence of fiber bridging. Surface analysis is recommended to confirm this observation. Furthermore, further investigation is warranted as variations in the incision (sharpened crack tip) using different tools and techniques may affect the results.

It is important to note that the fabrication of the notch alignment with respect to the interlayer plane had limited control due to the constraints of waterjet fabrication. Measurements were taken around these features, including the placement of loading pins, to explore any correlation or trends that may arise in the future. Some specimens exhibited tilt as they reached stability, which can be attributed to inconsistencies in fabrication, particularly in waterjet cutting. The misalignment of the interlayer with the notch and loading pin holes introduces undesired shear loads that are not accounted for in the calculations. This issue should be carefully considered.

Furthermore, it should be mentioned that the corrector fluid used did not dry quickly enough before testing. While this may not be problematic for other types of testing relying on markings, it had a significant impact on a few tests in this study. The viscosity of the corrector fluid posed difficulties in capturing the crack propagation in the video analysis, even as the crack extended. This issue was addressed by drying each specimen with a fan immediately after removal from the conditioning chamber. Although this proved to be a suitable solution, it deviated from the conditioning standards. For future reference, alternative solutions are proposed, such as using a dry white paint or powder-based primer that would provide sufficient contrast on the specimen and eliminate the need for drying. Another option is to apply the coating before conditioning. Additionally, drying the material during conditioning, as a second option according to the standard, could be employed to dry the corrector fluid, making it brittle during testing.

6 Acknowledgement

7 References

[1] ASTM D256-10, 2018a. "Standard Test Methods for Determining the Izod Pendulum Impact Resistance of Plastics." ASTM International, West Conshohocken, PA. [WWW Document]. URL https://compass.astm.org/document/?contentCode=ASTM%7CD0256-10R18%7Cen-US (accessed 3.20.23).

[2] ASTM D3039/3039M, 2017a. "Standard Test Method for Tensile Properties of Polymer Matrix Composite Materials." ASTM International, West Conshohocken, PA [WWW Document]. URL https://compass.astm.org/document/?contentCode=ASTM%7CD3039_D3039M-17%7Cen-US&proxycl=https%3A%2F%2Fsecure.astm.org&fromLogin=true (accessed 3.20.23).

[3] ASTM D5528, 2021a. "Standard Test Method for Mode I Interlaminar Fracture Toughness of Unidirectional Fiber-Reinforced Polymer Matrix Composites." ASTM International, West Conshohocken, PA. [WWW Document]. URL https://www.astm.org/d5528_d5528m-21.html (accessed 1.17.23).

[4] ASTM D6110-18, 2018b. "Standard Test Method for Determining the Charpy Impact Resistance of Notched Specimens of Plastics." ASTM International, West Conshohocken, PA. [WWW Document]. URL https://compass.astm.org/document/?contentCode=ASTM%7CD6110-18%7Cen-US&proxycl=https%3A%2F%2Fsecure.astm.org&fromLogin=true (accessed 3.20.23).

[5] ASTM D618-21, 2021b. "Standard Practice for Conditioning Plastics for Testing." ASTM International, West Conshohocken, PA [WWW Document]. URL https://www.astm.org/d0618-21.html (accessed 3.20.23).

[6] ASTM D638-22, 2022. "Standard Test Method for Tensile Properties of Plastics." ASTM International, West Conshohocken, PA [WWW Document]. URL https://compass.astm.org/document/?contentCode=ASTM%7CD0638-22%7Cen-US (accessed 3.20.23).

[7] ASTM D790, 2017b. "Standard Test Methods for Flexural Properties of Unreinforced and Reinforced Plastics and Electrical Insulating Materials." ASTM International, West Conshohocken, PA [WWW Document]. URL https://compass.astm.org/document/?contentCode=ASTM%7CD0790-17%7Cen-US (accessed 3.9.23).

[8] Billah, K.M.M., Lorenzana, F.A.R., Martinez, N.L., Wicker, R.B., Espalin, D., 2020. Thermomechanical characterization of short carbon fiber and short glass fiber-reinforced ABS used in large format additive manufacturing. Additive Manufacturing 35, 101299. https://doi.org/10.1016/j.addma.2020.101299

[9] Borish, M., Post, B.K., Roschli, A., Chesser, P.C., Love, L.J., Gaul, K.T., Sallas, M., Tsiamis, N., 2019. In-Situ Thermal Imaging for Single Layer Build Time Alteration in Large-Scale

Polymer Additive Manufacturing. Procedia Manufacturing, 47th SME North American Manufacturing Research Conference, NAMRC 47, Pennsylvania, USA. 34, 482–488. https://doi.org/10.1016/j.promfg.2019.06.202

[10] Caltagirone, P.E., Cousins, D.D., Snowberg, D., Stebner, D.A.P., 2020. DETERMINING MODE I FRACTURE TOUGHNESS OF ADHESIVE COMPOSITE JOINTS: AUTONOMOUS CRACK TRACKING USING MATLAB DEVELOPED PROGRAM.

[11] Colón Quintana, J.L., Slattery, L., Pinkham, J., Keaton, J., Lopez-Anido, R.A., Sharp, K., 2022. Effects of Fiber Orientation on the Coefficient of Thermal Expansion of Fiber-Filled Polymer Systems in Large Format Polymer Extrusion-Based Additive Manufacturing. Materials 15, 2764. https://doi.org/10.3390/ma15082764

[12] Curran, S., Chambon, P., Lind, R., Love, L., Wagner, R., Whitted, S., Smith, D., Post, B., Graves, R., Blue, C., Green, J., Keller, M., 2016. Big Area Additive Manufacturing and Hardware-in-the-Loop for Rapid Vehicle Powertrain Prototyping: A Case Study on the Development of a 3-D-Printed Shelby Cobra. Presented at the SAE 2016 World Congress and Exhibition, pp. 2016-01–0328. https://doi.org/10.4271/2016-01-0328

[13] Davies, P., Benzeggagh, M.L., 1989. Chapter 3 - Interlaminar Mode-I Fracture Testing, in: Friedrich, K. (Ed.), Composite Materials Series, Application of Fracture Mechanics to Composite Materials. Elsevier, pp. 81–112. https://doi.org/10.1016/B978-0-444-87286-9.50007-3

[14] Duty, C., Love, L., 2015. Cincinnati Big Area Additive Manufacturing (BAAM) (No. ORNL/TM-2015/100, 1210140, CRADA/NFE-14-04957). https://doi.org/10.2172/1210140

[15] Forster, A.M., 2015. Materials Testing Standards for Additive Manufacturing of Polymer Materials: State of the Art and Standards Applicability (No. NIST IR 8059). National Institute of Standards and Technology. https://doi.org/10.6028/NIST.IR.8059

[16] Greenhalgh, E., 2009. Failure Analysis and Fractography of Polymer Composites. Elsevier.

[17] Hill, C., Bedsole, R., Rowe, K., Duty, C., Ajinjeru, C., Kunc, V., Riha, D., 2018. Big Area Additive Manufacturing (BAAM) Materials Development and Reinforcement with Advanced Composites (No. IACMI/-0015-2017/3.6). Inst. for Advanced Composites Manufacturing Innovation (IACMI), Knoxville, TN (United States). https://doi.org/10.2172/1434289

[18] Khan, R., 2019. Fiber bridging in composite laminates: A literature review. Composite Structures 229, 111418. https://doi.org/10.1016/j.compstruct.2019.111418

[19] Kinloch, A.J., Shaw, S.J., Tod, D.A., Hunston, D.L., 1983. Deformation and fracture behaviour of a rubber-toughened epoxy: 1. Microstructure and fracture studies. Polymer 24, 1341–1354. https://doi.org/10.1016/0032-3861(83)90070-8

[20] Kishore, V., Ajinjeru, C., Nycz, A., Post, B., Lindahl, J., Kunc, V., Duty, C., 2017. Infrared preheating to improve interlayer strength of big area additive manufacturing (BAAM) components. Additive Manufacturing 14, 7–12. https://doi.org/10.1016/j.addma.2016.11.008

[21] Kumar, V., Alwekar, S.P., Kunc, V., Cakmak, E., Kishore, V., Smith, T., Lindahl, J., Vaidya, U., Blue, C., Theodore, M., Kim, S., Hassen, A.A., 2021. High-performance molded composites using additively manufactured preforms with controlled fiber and pore morphology. Additive Manufacturing 37, 101733. https://doi.org/10.1016/j.addma.2020.101733

[22] Meraz Trejo, E., Jimenez, X., Billah, K.M.M., Seppala, J., Wicker, R., Espalin, D., 2020. Compressive deformation analysis of large area pellet-fed material extrusion 3D printed parts in relation to in situ thermal imaging. Additive Manufacturing 33, 101099. https://doi.org/10.1016/j.addma.2020.101099

[23] Mostovoy, S., Crosley, P., Ripling, E., 1967. Use of Crack-Line-Loaded Specimens for Measuring Plane-Strain Fracture Toughness. Journal of Materials 2, 661-.

[24] Musio-Sale, M., Nazzaro, P.L., Peterson, E., 2020. Visions, Concepts, and Applications in Additive Manufacturing for Yacht Design, in: Di Nicolantonio, M., Rossi, E., Alexander, T. (Eds.), Advances in Additive Manufacturing, Modeling Systems and 3D Prototyping, Advances in Intelligent Systems and Computing. Springer International Publishing, Cham, pp. 401–410. https://doi.org/10.1007/978-3-030-20216-3_37

[25] Nestor Perez, 2004. 6 The Energy Principle, in: Fracture Mechanics. Springer, Boston.

[26] Nycz, A., Kishore, V., Lindahl, J., Duty, C., Carnal, C., Kunc, V., 2020. Controlling substrate temperature with infrared heating to improve mechanical properties of large-scale printed parts. Additive Manufacturing 33, 101068. https://doi.org/10.1016/j.addma.2020.101068

[27] Pappas, J.M., Thakur, A.R., Leu, M.C., Dong, X., 2021. A Comparative Study of Pellet-Based Extrusion Deposition of Short, Long, and Continuous Carbon Fiber-Reinforced Polymer Composites for Large-Scale Additive Manufacturing. Journal of Manufacturing Science and Engineering 143. https://doi.org/10.1115/1.4049646

[28] Ripling, E.J., Mostovoy, S., Corten, H.T., 1971. Fracture Mechanics: A Tool for Evaluating Structural Adhesives. The Journal of Adhesion 3, 107–123. https://doi.org/10.1080/00218467108081158

[29] Schnittker, K., Arrieta, E., Jimenez, X., Espalin, D., Wicker, R.B., Roberson, D.A., 2019. Integrating digital image correlation in mechanical testing for the materials characterization of big area additive manufacturing feedstock. Additive Manufacturing 26, 129–137. https://doi.org/10.1016/j.addma.2018.12.016

[30] Smiley, A.J., Pipes, R.B., 1987. Rate Effects on Mode I Interlaminar Fracture Toughness in Composite Materials. Journal of Composite Materials 21, 670–687. https://doi.org/10.1177/002199838702100706

[31] Spoerk, M., Savandaiah, C., Arbeiter, F., Traxler, G., Cardon, L., Holzer, C., Sapkota, J., 2018. Anisotropic properties of oriented short carbon fibre filled polypropylene parts fabricated by extrusion-based additive manufacturing. Composites Part A: Applied Science and Manufacturing 113, 95–104. https://doi.org/10.1016/j.compositesa.2018.06.018

[32] Spreeman, M.E., Stretz, H.A., Dadmun, M.D., 2019. Role of compatibilizer in 3D printing of polymer blends. Additive Manufacturing 27, 267–277. https://doi.org/10.1016/j.addma.2019.03.009

[33] Winter, K., Wilfert, J., Häupler, B., Erlmann, J., Altstädt, V., 2022. Large Scale 3D Printing: Influence of Fillers on Warp Deformation and on Mechanical Properties of Printed Polypropylene Components. Macromolecular Materials and Engineering 307, 2100528. https://doi.org/10.1002/mame.202100528

[34] Yamawaki, M., Kouno, Y., 2018. Fabrication and mechanical characterization of continuous carbon fiber-reinforced thermoplastic using a preform by three-dimensional printing and via hot-press molding. Advanced Composite Materials 27, 209–219. https://doi.org/10.1080/09243046.2017.1368840

[35] Yang, D., Zhang, H., Wu, J., McCarthy, E.D., 2021. Fibre flow and void formation in 3D printing of short-fibre reinforced thermoplastic composites: An experimental benchmark exercise. Additive Manufacturing 37, 101686. https://doi.org/10.1016/j.addma.2020.101686

[36] Yeole, P., Kim, S., Hassen, A.A., Kumar, V., Kunc, V., Vaidya, U., 2021. Large-scale additive manufacturing tooling for extrusion-compression molds. Additive Manufacturing Letters 1, 100007. https://doi.org/10.1016/j.addlet.2021.100007

[37] Young, D., Wetmore, N., Czabaj, M., 2018. Interlayer fracture toughness of additively manufactured unreinforced and carbon-fiber-reinforced acrylonitrile butadiene styrene. Additive Manufacturing 22, 508–515. https://doi.org/10.1016/j.addma.2018.02.023